

Spaceborne Doppler Radar Measurements of Rainfall: Correction of Errors Induced by Pointing Uncertainties

SIMONE TANELLI, EASTWOOD IM, AND SATORU KOBAYASHI

Jet Propulsion Laboratory, California Institute of Technology, Pasadena, California

ROBERTO MASCELLONI AND LUCA FACHERIS

Dipartimento Elettronica e Telecomunicazioni, Università di Firenze, Firenze, Italy

(Manuscript received 15 December 2004, in final form 14 March 2005)

ABSTRACT

In this paper a sea surface radar echo spectral analysis technique to correct for the rainfall velocity error caused by radar-pointing uncertainty is presented. The correction procedure is quite straightforward when the radar is observing a homogeneous rainfall field. When nonuniform beam filling (NUBF) occurs and attenuating frequencies are used, however, additional steps are necessary in order to correctly estimate the antenna-pointing direction. This new technique relies on the application of the combined frequency–time (CFT) algorithm to correct for uneven attenuation effects on the observed sea surface Doppler spectrum. The performance of this correction technique was evaluated by a Monte Carlo simulation of the Doppler precipitation radar backscatter from high-resolution 3D rain fields (either generated by a cloud resolving numerical model or retrieved from airborne radar measurements). The results show that the antenna-pointing-induced error can, indeed, be reduced by the proposed technique in order to achieve 1 m s^{-1} accuracy on rainfall vertical velocity estimates.

1. Introduction

Knowledge of the global distribution of the vertical rainfall velocity is important in estimating latent heat fluxes, and in the study of energy transportation in the atmosphere. The vertical velocity signature of different hydrometeors is also very useful in classifying precipitating systems (e.g., rain versus snow, convective versus stratiform). Such knowledge can only be acquired with the use of spaceborne Doppler precipitation radars.

Although the high relative speed of an orbiting radar with respect to the rainfall particles introduces significant broadening in the Doppler spectrum, recent studies (Tanelli et al. 2002, 2004) have proven that the average vertical velocity can indeed be measured to the 1 m s^{-1} accuracy level by the proper selection of radar parameters. The parameters and configuration for a representative 14-GHz nadir-pointing spaceborne

Doppler precipitation radar (NDPR; see appendix C for a complete list of acronym and symbol definitions) employed in this study are shown in Table 1. In the aforementioned papers the radar was assumed to be looking exactly at nadir; in this paper, we focus our attention on the error component in vertical rainfall velocity estimation introduced by an unknown off-nadir-pointing error. As discussed through a quantitative example in section 2, the pointing error budgets that are required to obtain acceptable errors in vertical velocity estimates are extremely tight. The objective of this paper is to describe a processing algorithm, which provides the required level of pointing knowledge without the need of imposing a tight requirement on spaceborne instrumentations. The algorithm is based on the basic principle that, assuming an antenna pattern symmetric in the along-track direction (here it is assumed to be 2D Gaussian within the main lobe and circularly symmetric) and nadir viewing geometry, the ocean surface is expected to have a zero average radial velocity over the radar footprint. As such, any apparent nonzero average vertical velocity resulting from pointing-induced bias should be removed from vertical velocity

Corresponding author address: Simone Tanelli, Mail Stop 300-243, Jet Propulsion Laboratory, 4800 Oak Grove Drive, Pasadena, CA 91109.
E-mail: simone.tanelli@jpl.nasa.gov

TABLE 1. System configuration parameters of NDPR. This representative configuration differs significantly from TRMM configuration only in the antenna size (2.2 m for TRMM) and in the added Doppler capability.

v_s	7 km s ⁻¹
h_s	432 km
PRF	7000 Hz
f_c	13.6 GHz
θ_{3dB}	0.3°
M	64
Equivalent noise	10 dBZ

estimates at range cells above the surface. This approach is similar to the use of clutter-lock procedures to determine the Doppler center frequency in synthetic aperture radar (SAR) imaging (Curlander and McDonough 1991). In vertical rainfall velocity estimation, however, one must take into account the attenuation of the radar pulse traveling through the rainy atmosphere, which, at 14 GHz, can be quite significant at medium to heavy rain rates. Furthermore, under nonuniform beam filling (NUBF) conditions, in which the surface returns from different portions of the footprint are unevenly attenuated, additional considerations must be paid during the pointing error correction process because NUBF also causes the surface Doppler spectrum to have a nonzero mean, even if the radar is pointing exactly at nadir. The characteristics of the sea surface Doppler spectrum are described in section 3 of this paper, with further details about the received signal being provided in appendix A and the references cited therein.

In section 4, the application of the combined frequency-time (CFT) algorithm to sea surface Doppler spectra is described. The CFT algorithm, originally developed to correct for the NUBF-induced bias in vertical velocity measurements of rainfall (Tanelli et al. 2004), is applied in this paper also to analyze the sea surface Doppler spectrum and correct for the pointing-induced bias in vertical velocity under uniform beam filling (UBF) and nonuniform beam filling conditions.

2. Effect of pointing errors on vertical velocity estimates

Figure 1 shows the geometry of the problem and introduces the vector notation used throughout this paper. The main Cartesian reference system is defined so that the unit vector \mathbf{i}_x indicates the along-track direction (i.e., the local projection of the spacecraft trajectory on the earth surface), and \mathbf{i}_z is toward the zenith so that x - z is the orbital plane and y - z is the cross-track plane. A second reference system is defined with re-

spect to the spacecraft instantaneous motion: \mathbf{i}_M is the unit vector in the satellite motion direction, and \mathbf{i}_N is orthogonal to \mathbf{i}_M and points downward; both lie on the orbital plane. The unit vectors $\mathbf{i}_C = -\mathbf{i}_y$ complete the two reference systems. In general, the satellite position \mathbf{p}_s over a time interval of a few seconds can be approximated as $\mathbf{p}_s(t) = [x_s(t), 0, h_s + v_s t \sin(\theta_A)]$, where $x_s(t) = v_s t \cos(\theta_A)$ is the satellite along-track position at time t , v_s is the satellite speed, and h_s is the satellite altitude at initial time. If the spacecraft is moving parallel to the local tangent to the earth surface (i.e., $\theta_A = 0$), then $\mathbf{i}_M = \mathbf{i}_x$ and $\mathbf{i}_N = -\mathbf{i}_z$. The unit vector in the antenna-pointing direction (i.e., the pointing vector) \mathbf{i}_V can be represented in spherical coordinates as $\{1, \theta_V, \phi_V\}$, where \mathbf{i}_N is the z axis of this spherical coordinate system (i.e., $\theta = 0$). The center of the resolution volume is indicated by $\mathbf{r}_V = r_V \mathbf{i}_V$. Finally, $\mathbf{r} = r \mathbf{i}_R = (r, \theta, \phi)$ represents a generic position with respect to the satellite.

For a moving rain target at position \mathbf{r} and with velocity vector \mathbf{u} , its apparent radial velocity v_r can be written as

$$v_r = \mathbf{u} \cdot \mathbf{i}_R - v_s \mathbf{i}_M \cdot \mathbf{i}_R. \quad (1)$$

Note that a negative v_r indicates that the target is moving toward the radar. The first term in the right-hand side of Eq. (1) is the radar line-of-sight component of the target velocity. For NDPR, it corresponds to the vertical velocity (because $\mathbf{i}_z \cdot \mathbf{i}_R \approx 1$). The second term represents the radial velocity offset resulting from the velocity of the spacecraft. Its contribution cannot be ignored, even for a nadir-looking system (where $\mathbf{i}_M \cdot \mathbf{i}_R \sim 0$), because v_s is typically ~ 7 km s⁻¹ for a low earth orbit (LEO) spacecraft, which is more than two orders of magnitude larger than the typical rainfall vertical velocity. This second term can be further divided, and Eq. (1) can be written as

$$v_r = \mathbf{u} \cdot \mathbf{i}_R - v_s \mathbf{i}_M \cdot (\mathbf{i}_R - \mathbf{i}_V) + v_P. \quad (2)$$

The second term in Eq. (2) represents the radial velocity offset resulting from the displacement of the target position relative to the center of the radar resolution volume. In the case of a distributed target, such as rainfall, it gives rise to the broadening of the Doppler spectrum under UBF conditions (Meneghini and Kozu 1990; Amayenc et al. 1993; and Kobayashi 2002), as well as to the bias introduced by NUBF in the retrieval of vertical rainfall velocity (Tanelli et al. 2002).

The last term in Eq. (2), $v_P = -v_s \mathbf{i}_M \cdot \mathbf{i}_V$, is the pointing-induced bias in vertical velocity. It affects velocity estimates from all radar volumes of resolution in the line of sight given by \mathbf{i}_V , including that intersecting the earth surface. For a nadir-pointing or a cross-track-

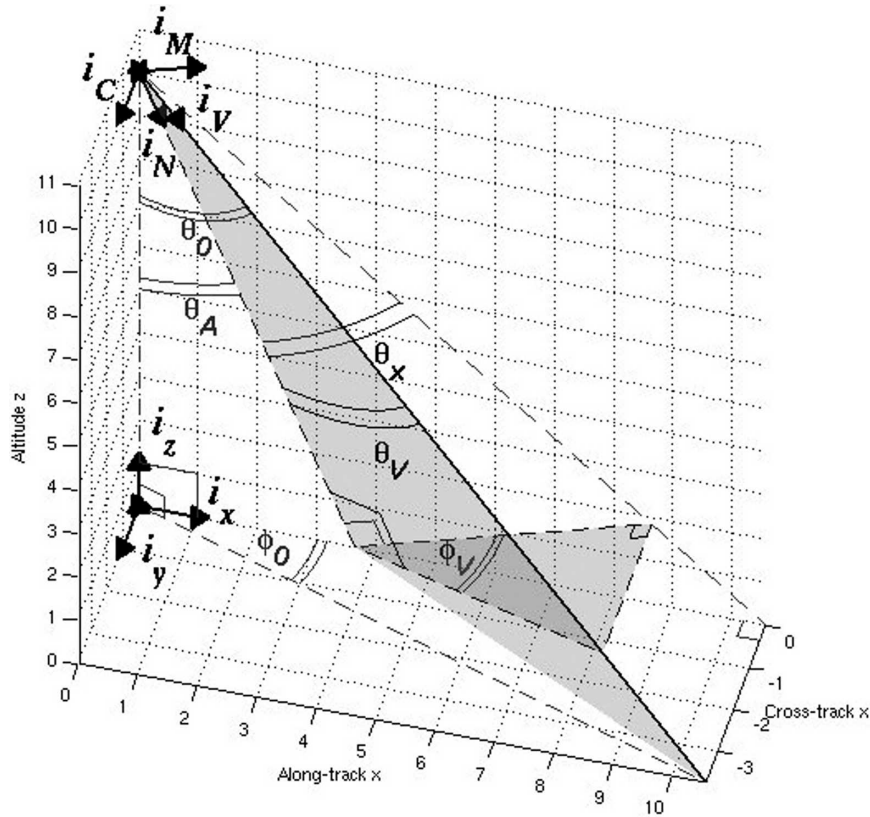


FIG. 1. Schematic of geometry of the problem: θ_A is the angle between the actual spacecraft motion vector and its ground projection, θ_V and ϕ_V are the elevation and azimuth angles of the radar beam with respect to the spacecraft motion, θ_0 and ϕ_0 are the elevation and azimuth angles of the radar beam with respect to the earth reference system, and θ_x is the forward-aft component of the radar beam-pointing angle.

scanning atmospheric radar with no pointing error in the forward-aft direction (i.e., $\mathbf{i}_V \cdot \mathbf{i}_M = 0$), this term is zero. In actuality, however, several factors, such as attitude determination errors, thermal distortions of the antenna structure, vibrations resulting from moving parts, slew, thermal flutter, or thermal snaps at the eclipse border line for a LEO satellite, etc., can cause error in radar pointing. The scalar product $\mathbf{i}_V \cdot \mathbf{i}_M$ can be defined in terms of the antenna elevation and azimuth angles θ_V and ϕ_V :

$$v_P = -v_s \sin(\theta_V) \cos(\phi_V). \quad (3)$$

A complete derivation of Eq. (3), including coherent and incoherent scattering phenomena, is found in appendix B, in which the angles θ_0 and ϕ_0 , defined in the spherical reference system with the z axis along $-\mathbf{i}_z$ rather than along \mathbf{i}_N , are used (i.e., including the uncertainty on θ_A). Notice that Eq. (3) holds true whenever the coherent scattering is negligible. Furthermore, Eq. (3) can be expressed in terms of the forward-aft com-

ponent θ_x (i.e., the angle between \mathbf{i}_N and the projection of \mathbf{i}_V on the orbital plane, which is positive forward) as

$$v_P = -v_s \sin(\theta_x) \sqrt{1 - \sin^2(\theta_V) \sin^2(\phi_V)}; \quad (4)$$

for small θ_V or ϕ_V the term under square root is close to 1 and the velocity bias can be expressed as function of θ_x only:

$$v_P \cong -v_s \sin(\theta_x). \quad (5)$$

For this reason, in the following we will focus on the forward-aft-pointing error only. In practice, the pointing error is required to be less than the radar beam-width, which is less than 1° for NDPR; therefore, Eq. (5) can be further reduced to $v_P \cong -v_s \theta_x$.

In general, θ_A is well known from ephemeris information, however, even if uncertainty is present on its estimate, it translates in an uncertainty on the georeference of measurements and not on Doppler velocity measurements. Only if one was to define the mispointing angles as θ_0 and ϕ_0 , then Eq. (47) in Kobayashi and

Kumagai (2003) should be used to account for the uncertainty on θ_A .

The radar-pointing angle θ_x can be divided in pointing control error θ_C and pointing uncertainty θ_α :

$$\theta_x = \theta_C + \theta_\alpha. \quad (6)$$

The pointing control error θ_C is the angle between the nominal (desired; in NDPR case it is at nadir) pointing vector and the pointing vector estimated by the spacecraft's attitude determination system (ADS). Provided that such an off-nadir angle is known, the bias in vertical velocity estimates resulting from the presence of this pointing angle offset can easily be accounted for through Eq. (3), and corrected for by using the spacecraft navigational data. For this reason, in this paper, we do not address requirements on the pointing control error.

The pointing uncertainty θ_α is the angle between the actual radar-pointing vector and the pointing vector estimated by the ADS. For the NDPR, the pointing uncertainty budget needs to be more stringent than those for non-Doppler radars. In fact, given a typical science requirement of 1 m s^{-1} accuracy in vertical rainfall velocity estimates, the requirement on the unknown portion $v_\alpha = -v_s \theta_\alpha$ of the pointing-induced bias must be less than 1 m s^{-1} . In fact, assuming that the error introduced by the pointing uncertainty is independent of all other sources of error, and modeling all errors as random variables with Gaussian distribution, one can simply sum their variance to obtain the overall variance of the estimate. For example, it was shown in Tanelli et al. (2004) that a root-mean-square error (rmse) better than 0.75 m s^{-1} on vertical velocity estimates can be obtained by NDPR for a signal-to-noise ratio (SNR) $> 10 \text{ dB}$ and by ignoring pointing errors. To satisfy the 1 m s^{-1} overall requirement, one should impose $\text{rms}(v_\alpha) < 0.66 \text{ m s}^{-1}$. For a satellite velocity $v_s \cong 7 \text{ km s}^{-1}$, this is equivalent to a pointing requirement of uncertainty less than $\sigma_\alpha = \text{rms}(\theta_\alpha) = \arcsin[\text{rms}(v_\alpha)/v_s] \cong 0.0055^\circ \cong 20 \text{ arcsec}$, which is two orders of magnitude smaller than the antenna 3-dB beamwidth θ_3 . Such a pointing uncertainty budget for a satellite poses a technological challenge, even for the most sophisticated ADS (see, e.g., Sabelhaus et al. 2001; Sirota et al. 2001; Voth et al. 2001; Wertz and Larson 1999).

A third component of a pointing error budget is the pointing stability σ_β , defined as the rms change in pointing angle θ_x over a certain time interval (or, equivalently, an angle change rate)

$$\sigma_\beta = \left[\int_t^{t+T_I} |\theta_x(t) - \langle \theta_x(t) \rangle|^2 dt \right]^{0.5}, \quad (7)$$

where the $\langle \rangle$ operator indicates averaging over the same time interval T_I . In general, T_I is defined as the observation time during which data are collected to obtain a single estimate for a given instrument. For NDPR, T_I is the time needed to obtain one estimate of mean Doppler velocity; M radar pulses are used to obtain each vertical velocity estimate, therefore, the observation time is $T_I = M/\text{PRF} \cong 0.01 \text{ s}$, where PRF is the pulse repetition frequency, and the spectral resolution of the Doppler spectrum is $\Delta v = \text{PRF} \lambda/(2M) \cong 1 \text{ m s}^{-1}$, where λ is the operating wavelength.

It is desirable that the observed process be stationary during T_I (e.g., the spectral signature of each scatterer does not vary by more than $\pm \Delta v$ within T_I). Therefore, assuming a Gaussian distribution for θ_β , one can impose the standard deviation of pointing-induced bias $v_\beta = -v_s \theta_\beta$ to be less than $\Delta v/3$, or

$$v_s \sigma_\beta < \frac{1}{3} \frac{\lambda \text{PRF}}{2M}. \quad (8)$$

The right-hand term of Eq. (8) is 0.33 m s^{-1} for the NDPR configuration considered here. In other words, the pointing stability requirement for NDPR equals half the pointing uncertainty requirement, but only over an interval $T_I = 0.01 \text{ s}$.

The temporal characteristics of the random process $\theta_x(t)$ are generally defined through its power spectrum $\Theta(f)$, which results from several different torque sources (both external to the spacecraft, such as the drag, and internal to the spacecraft, such as the spacecraft attitude controller itself). In general, such a spectrum (hereinafter referred to as "torque spectrum") has a "low pass" shape with a bandwidth B_Θ up to only a few hertz (Lee et al. 2002). While the pointing stability is affected only by the portion of the torque spectrum that is above the cutoff frequency $f_I = 1/T_I$, the whole spectrum contributes to the pointing uncertainty. Therefore, in practice, the σ_β requirement is not as stringent as σ_α , because most of the energy of the spectrum $\Theta(f)$, does not contribute to the short-term instability generated by the portion of $\Theta(f)$ above $f_I = 1/T_I = 100 \text{ Hz}$.

In the following, we shall focus on the pointing uncertainty error $\theta_\alpha(t)$ and its temporal evolution at time scales larger than T_I [i.e., the following assumptions are made $\theta_C = 0$, $\text{rms}(\theta_x) < \sigma_\beta/2$ within T_I].

3. Doppler spectrum of the sea surface

A viable alternative to imposing a very tight pointing uncertainty requirement σ_α is to estimate the pointing-induced bias v_p in velocity estimates by analyzing the Doppler spectrum of the sea surface backscatter signal in order to estimate the sea surface apparent velocity v_{surf} .

For a narrowbeam spaceborne radar pointing close to nadir, such as NDPR, the volumes of resolution in the troposphere can be well approximated by cylinders with vertical axis. Therefore, the Doppler spectrum of the sea surface for a satellite located at $\mathbf{p}_s = (x_s, y_s, h_s)$ can be expressed as

$$P(x_s, v) = W_Z(z_V) \int_{-\infty}^{+\infty} \int_{-\infty}^{+\infty} \eta(x, y; v - q_{xv}x') \times 10^{-0.2 \int k(x, y, z) dz} W_X(x - x_V) W_Y(y - y_V) dx dy, \quad (9)$$

where $x' = \mathbf{r} \cdot \mathbf{i}_M$ is the along-track displacement (from the zero Doppler curve) of the generic point at coordinate x in the main Cartesian reference system; $q_{xv} \equiv v_s/h_s$ is the rate of Doppler shift; $q_{xv}x'$ is the Doppler velocity shift as obtained through (5); $\eta(x, y; v)$ is the sea surface natural Doppler velocity spectrum (i.e., the sea surface spectrum that would be observed from a nonmoving, nadir-pointing instrument); $k(x, y, z)$ is the specific attenuation in decibels per kilometer induced by the hydrometeors above the surface; $(x_V, y_V, 0)$ are the coordinates of the center of the footprint; $W_X(x)$ and $W_Y(y)$ are the two-way-antenna pattern-weighting functions in the along- and cross-track directions, respectively; and $W_Z(z)$ is the radar range-weighting function (which includes here the radar constant).

The natural Doppler spectrum $\eta(x, y; v)$ can also be written as

$$\eta(x, y; v) = C_0 \sigma_0(x, y) \eta_N(v), \quad (10)$$

where $\sigma_0(x, y)$ is the normalized radar cross section of the surface,

$$C_0 \sigma_0(x, y) = \int_{-\infty}^{+\infty} \eta(x, y; v) dv, \quad (11)$$

and $\eta_N(v)$ is the normalized natural Doppler spectrum of the surface. For a nadir-pointing radar, the spectral shape of $\eta_N(v)$ is determined by the different vertical velocities of the sea surface; therefore, it has, in general, a zero mean with spectral width of less than 1 m s^{-1} . A detailed description of the characteristics of the radar signal returned from the sea surface is provided in appendix A and the corresponding references.

For NDPR, $W_X(q_{xv}x)$ is approximately Gaussian with a width of $\sim 11 \text{ m s}^{-1}$ [i.e., one order of magnitude wider than $\eta_N(v)$]. Therefore, provided that $\sigma_0(x, y)$ and the distribution of total two-way vertical attenuation $A(x, y) = 10^{-0.2 \int k(x, y, z) dz}$ are homogeneous within the footprint (i.e., under UBF conditions), the radar Dopp-

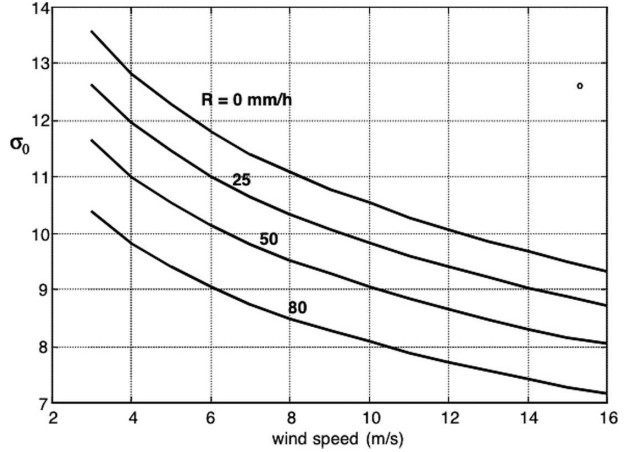


FIG. 2. Normalized radar cross section (dB) of the sea surface for a nadir-pointing radar at 14 GHz as a function of the wind speed at 20-m altitude and of the rain rate R at the surface. Results are calculated through a full-wave model (FWM) scattering model of the sea surface.

ler spectrum $P(x_s, v)$ is Gaussian and centered at $v_P = -q_{xv}x'_V$. That is, $v_{\text{surf}} = v_P$. However, this is not the case in general because of the variability in both σ_0 and A within the radar resolution volume. At a given frequency, σ_0 depends on incidence angle, surface wind speed u_{surf} , wind speed direction, and surface rain rate R . At 14 GHz and near-nadir incidence angles, the dependence of σ_0 on the incidence angle is rather weak (e.g., less than 0.1 dB for angles within 1° from nadir), and the dependence on wind direction is negligible. On the other hand, the dependence of σ_0 on rain rate R and wind speed u_{surf} are more pronounced. Figure 2 plots σ_0 against u_{surf} for four values of R for a nadir-looking radar at 14 GHz. These results were generated using a full-wave model described in Capolino et al. (1998) in which the sea surface is characterized by the wind spectrum from Apel (1994) and by the ring waves generated by the raindrops. Note that at nadir, σ_0 for 20 mm h^{-1} rain is almost 1 dB below that for a clear ocean. As discussed in the next section, the impact of the total attenuation $A(x, y)$ at 14 GHz is even more evident and, therefore, the backscattered power from the surface decreases proportionally to the rain rate present above it because of the joint effect of a larger $A(x, y)$ and lower $\sigma_0(x, y)$. Under NUBF conditions, $\sigma_0(x, y)$ and $A(x, y)$ are not homogeneous across the radar footprint, and, therefore, (9) cannot be interpreted anymore as the convolution of a zero-mean Gaussian with a Gaussian centered on $v_P = -q_{xv}x'_V$. Consequently, the spectrum is no longer Gaussian and is not centered on v_P . That is, the sea surface apparent velocity v_{surf} does not necessarily correspond to the pointing-induced bias in vertical velocity estimates v_P , but it includes a second

bias dependent on the distribution of rainfall in the along-track direction inside the antenna main lobe.

4. Estimation of the sea surface apparent velocity

a. Estimation of sea surface apparent velocity through spectral moment estimators

Under UBF conditions, the pointing-induced bias v_p in vertical velocity measurements defined by Eq. (3) can be obtained simply by estimating the first moment of the measured Doppler spectrum of the sea surface. Several spectral moment estimators are currently available for treating Gaussian spectra. The two most widely used in atmospheric weather radar applications are the pulse pair (PP) and the discrete Fourier transform (DFT) methods (Zrnich 1979). The variance of the estimates of both estimators depends on several parameters, including the normalized spectral width $w_N = w/(\text{PRF } \lambda/2)$ (where w is the standard deviation of the Doppler spectrum, and $\text{PRF } \lambda/2$ is the unambiguous Doppler velocity range), the number of samples M , and the SNR. While PP provides better results for narrow spectra (e.g., $w_N < 0.1$), DFT performs better for spectra with normalized spectral widths ranging between 0.15 and 0.25, which are more applicable to spectra acquired by spaceborne Doppler radars (Tanelli et al. 2002). An estimate of the variance of DFT estimates of mean Doppler velocity can be calculated through (Zrnich 1979)

$$\text{var}(\hat{v}_p) \approx \frac{(\text{PRF} \cdot \lambda/2)^2}{M} \left[\frac{w_N}{4\sqrt{\pi}} + 2w_N^2 \frac{1}{\text{SNR}} + \frac{1}{12 \text{SNR}^2} \right]. \quad (12)$$

For NDPR configuration and large SNRs, M would need to be ~ 240 in order to estimate v_p with a standard deviation of 0.66 m s^{-1} , which corresponds to an observation time of about 0.04 s. This means that, in UBF conditions, this method can correct for the bias v_p induced by pointing errors generated by the portion of $\Theta(f)$ below 25 Hz.

As discussed in section 3, when NUBF occurs the apparent surface velocity v_{surf} does not always correspond to the pointing-induced bias v_p . The sensitivity of the former to the NUBF-induced deformation of the spectrum can be evaluated for a simplified case where a uniform rain field with rain rate $= R_{\text{for}}$ fills the forward half of the radar beam and a uniform rain field with rain rate $= R_{\text{aft}}$ fills the aft half (see Fig. 3). That is, $R(x, y, z) = R_{\text{for}}$ for $x > x_s$ and $z \leq H$, $R(x, y, z) = R_{\text{aft}}$ for $x \leq x_s$ and $z \leq H$, and $R(x, y, z) = 0$ for $z > H$, where

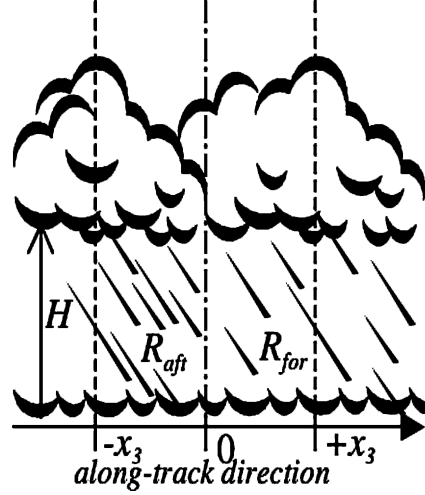


FIG. 3. Simplified model to estimate impact of NUBF.

H is the thickness of the rainy layer. By writing the specific attenuation as $k = a R^b$, one obtains the total attenuation in the forward (A_{for}) and aft (A_{aft}) halves of the footprint through

$$A_i = 10^{-0.2HaR_i^b}, \quad (13)$$

where $i = \text{aft or forward}$. Assuming a Gaussian antenna pattern, the first moment of the surface spectrum for NDPR can be written as

$$\begin{aligned} v_{\text{surf}} &= v_p + q_{xv} \sqrt{\frac{2}{\pi}} \frac{x_3}{2\sqrt{\ln(2)}} (A_{\text{aft}} - A_{\text{for}}) \\ &\equiv v_p + 0.24v_s\theta_3(A_{\text{aft}} - A_{\text{for}}), \end{aligned} \quad (14)$$

where $x_3 = h_s \tan(\theta_3/2)$ is the half-width of the 3-dB radar footprint. Although Eq. (14) is derived from a simplified model, it does provide some quantitative insight into assessing the impact of NUBF on antenna-pointing correction. As an example, let us represent a case of shallow, moderate precipitation and mild NUBF, with the following coefficients in Eq. (13): $a = 0.023$ and $b = 1.16$ (representative for Ku-band radar; Meneghini and Kozu 1990), $H = 2.5 \text{ km}$, $R_{\text{aft}} = 5 \text{ mm h}^{-1}$, and $R_{\text{for}} = 8 \text{ mm h}^{-1}$. It follows from Eq. (14) that a conventional spectral moment estimator would incur a NUBF-induced bias (additional to v_p) of about -0.7 m s^{-1} . Also, note that Eq. (14) was derived ignoring the dependence of σ_0 on the rain rate at the surface (discussed in section 3), which would further increase such bias.

A second simple model is useful to assess the effect of NUBF on the observed surface Doppler velocity: one could assume that the apparent (i.e., attenuated) surface reflectivity $Z_X(x)$, expressed in dBZ, varies linearly within the radar footprint. Following an approach

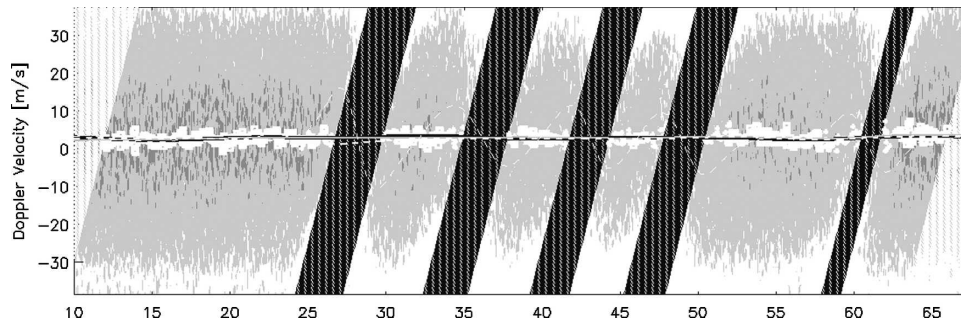


FIG. 4. CFT technique: an example of simulated sequence of measured Doppler spectra (periodograms) for the range bin intersecting the sea surface. The abscissa is the satellite along-track position x_s at which each periodogram was obtained. The power of a spectral line is expressed in equivalent radar reflectivity (i.e., the reflectivity that would result if all spectral lines in one periodogram were equal to that one).

similar to that used in the CFT (Tanelli et al. 2004) to correct for turbulence-induced offsets, one obtains

$$v_{\text{surf}} = -v_P - \frac{\ln(10)}{10} \frac{\partial Z_x(x)}{\partial x} \frac{w_{\text{UBF}}^2}{q_{xv}}, \quad (15)$$

where w_{UBF} is the Doppler spectral width in UBF conditions. Provided that an estimate of the along-track gradient of $Z_x(x)$ is available, the last term can be removed from the observed surface velocity to obtain v_P . The effectiveness of this approach to correct for the NUBF-induced bias is discussed in section 5.

Finally, the NUBF-induced distortion of the surface spectrum could be ignored by using only surface returns from clear-air measurements adjacent to the observed rainy area, and interpolating them to obtain a the pointing-induced bias inside the rainy area. However, in this case one should impose a second, more stringent, pointing stability budget by considering an observation time equal to L_r/v_s , where L_r is equal to the expected size of the largest rainfall event, instead of T_r , as calculated in section 2. For example, following the same approach used in section 1, by setting $L_r = 100$ km, one should increase pointing stability requirement by imposing a maximum rms equal to σ_β for all torque sources above $v_s/L_r \approx 0.07$ Hz. Summarizing the pointing stability budgets derived so far, we find that while only torque sources represented by the portion of $\Theta(f)$ above 100 Hz affect the measure of one spectrum of $M = 64$ samples, all of those above 25 Hz affect the observation of $M = 240$ samples, which are required to obtain an accurate measure of the sea surface vertical velocity in clear air (or UBF conditions); and, most hindering of all, the effect of torque sources all of the way down to few hundredths of a hertz could not be corrected by relying only on clear-air surface echoes. Indeed, while torque sources above 1 Hz could be dampened rela-

tively easily to fit the stability budget, this is not always the case for subhertz torque sources.

b. Estimation of sea surface apparent velocity through combined frequency–time technique

The CFT technique, described in Tanelli et al. (2004) and briefly recalled here, aims at removing the NUBF-induced bias from the estimates of rainfall average vertical velocity by estimating the first moment of the tracks of the rainfall distributed targets projected in the along-track satellite position/Doppler velocity (x – v) plane. Figure 4 shows a sequence of periodograms measured by a Doppler radar for the range cell intersecting the sea surface in the first case study discussed in section 5. Each periodogram is calculated from the DFT of M complex voltage samples. The example in Fig. 4 shows the effects of strong and nonuniform attenuation resulting from the presence of five rain cells embedded in the precipitating system shown in Fig. 5a. When NUBF occurs the power spectra deviate substantially from a Gaussian shape (e.g., at km 28). On the other hand, one can analyze the spectral density lines generated by a specific target at different times. The “target tracks” in the x – v plane are along lines with slope equal to the Doppler shift rate $q_{xv} = v_s/h_s$ (in Fig. 4, such a slope is visible as the slope of the blackout sections, that is, those portions where the signal was reduced by more than 20 dB with respect to the adjacent areas and, therefore, discarded by the estimation algorithm). It has been demonstrated that, for NDPR, the target tracks can be well approximated by a Gaussian (from the shape of the antenna pattern) with the same width w_{UBF} that a periodogram would have in UBF conditions, regardless of NUBF. Consequently, the first moment of each target track provides accurate information on both the target position (because the target is in the

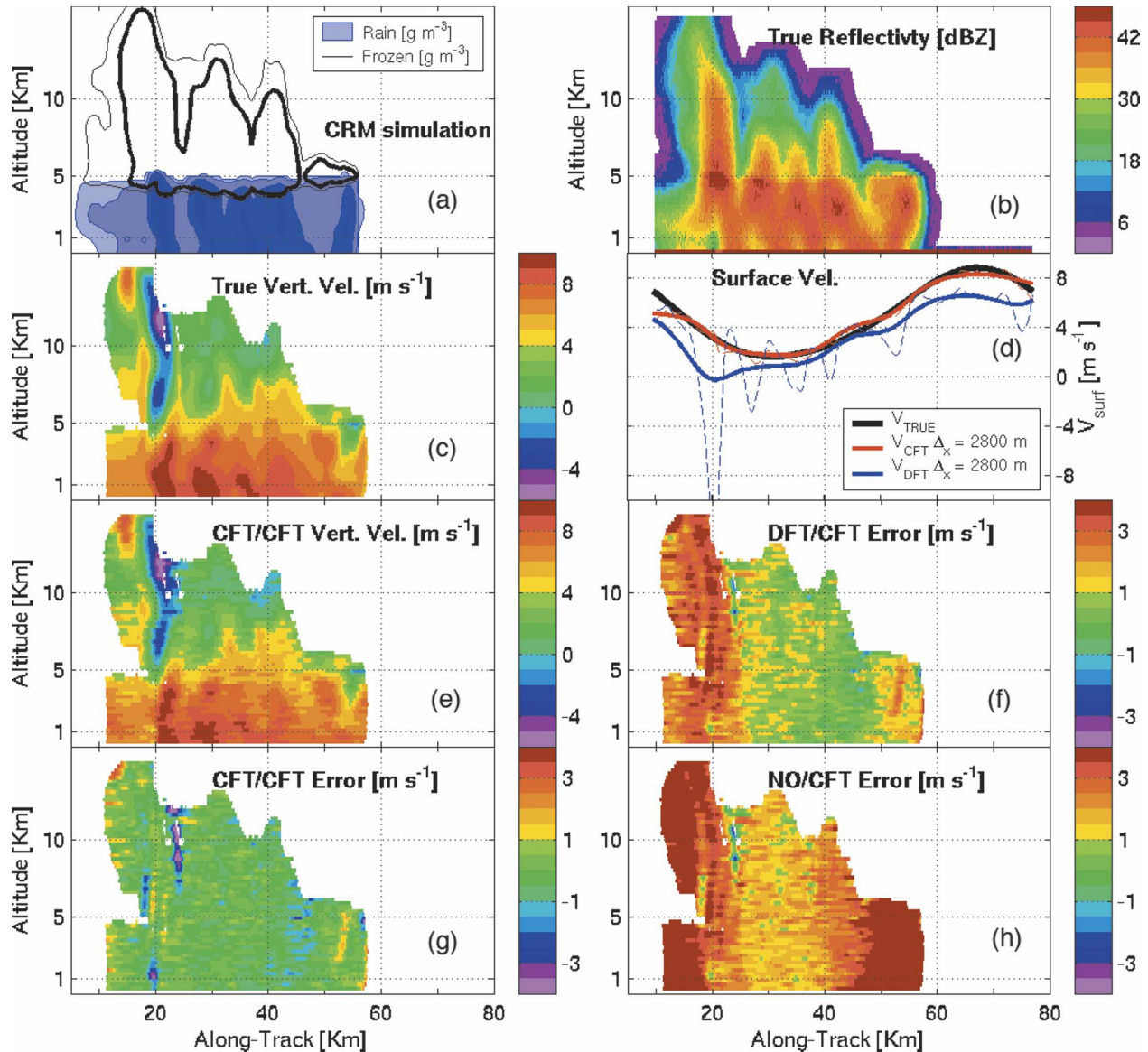


FIG. 5. Retrievals of vertical velocity from NDPR for a CRM-generated tropical storm: (a) equivalent mass liquid content for frozen hydrometeors (black, thin at 0.01 g m^{-3} and thick at 0.1 g m^{-3}) and rain (blue shades with transitions at 0.01 , 0.1 , 1 , and 3 g m^{-3}), (b) measured reflectivity, (c) true hydrometeor vertical velocity, (d) apparent surface velocity, (e) vertical velocity of hydrometeors estimated through the CFT/CFT approach, (f) error in vertical velocity estimates through the DFT/CFT approach, (g) error in vertical velocity estimates through the CFT/CFT approach, and (h) error in vertical velocity estimates through the NO/CFT approach.

antenna maximum gain direction), and the true line-of-sight velocity of the target (because the maximum gain direction is along \hat{i}_V). The variance of the vertical velocity estimates obtained from each target track can be calculated through Eq. (12) by replacing the number of samples per periodogram M with the number of samples per target track M_x [as defined by Eq. (8) in Tanelli et al. 2004]. The last step of the CFT technique consists in generating a uniformly spaced horizontal profile of vertical velocity through the weighted moving

average of the target velocities obtained for each target track. The moving average “along-track window” $D_m(x)$ is Gaussian shaped with width Δx . The variance of the velocity estimates can be reduced, with respect to that obtained through a single target track [i.e., that obtained through Eq. (12)], by choosing a Δx that is larger than the along-track spacing between consecutive target tracks and smaller than the horizontal decorrelation distance of the vertical velocity field.

The CFT can be applied to remove the NUBF-

induced bias from the sea surface return spectrum. In fact, because $\eta_N(v)$ is narrower than the rainfall natural Doppler spectrum, the approximation of each target track with a Gaussian whose width is determined by the antenna pattern is even more accurate. It is worth noting that such an approach holds true only for small antenna beamwidths and small values of $\mathbf{i}_V \cdot \mathbf{i}_M$, that is, when the “cylindrical” approximation used to calculate $A(x, y)$ in Eq. (9) is accurate. Incidentally, we note that this condition is not as stringent as that imposed on the antenna size by the requirement of correlation between two consecutive pulses; in other words, a spaceborne precipitation radar system on a LEO platform resulting in $w_N < 0.3$ has an antenna beamwidth that is narrow enough to satisfy the cylindrical approximation condition (Tanelli and Im 2004).

The CFT overcomes the effects of NUBF-induced biases on measures of the sea surface vertical velocity, and, therefore, allows for more frequent updates of the estimated pointing-induced bias. In particular, one can note that the along-track window $D_m(x)$ of the moving average performed at the end of the CFT algorithm acts as a low-pass Gaussian filter with 3-dB cutoff frequency $f_3 = (v_s/\Delta x)[\ln(2)/2\pi^2]^{1/2}$ in terms of spacecraft dynamics. Therefore, if the bandwidth B_Θ of the antenna oscillations can be estimated, the maximum size of $D_m(x)$ is given approximately by $\Delta x \approx (v_s/5.5B_\Theta)$. The approximation here is a result of the fact that the shape of the torque spectrum is, in general, not Gaussian, and is often unknown. In general, any information available on the torque spectrum can be used to define the optimum shape for $D_m(x)$, because, in principle, any family of low-pass filter impulse response function can be used for $D_m(x)$ in CFT. Assuming, for the sake of simplicity, a Gaussian shape for the torque spectrum, a cutoff frequency of the oscillations of $f_I = 1$ Hz, and the system configuration of Table 1, the choice of $\Delta x = 1300$ m will result in an optimal (i.e., matched) filtering that corresponds to averaging approximately over two radar footprints. Furthermore, assuming for the moment that (a) the estimates obtained from each target track within the window $D_m(x)$ are independent, (b) no significant portion of the oscillation is “filtered out” by the moving average, and (c) the attenuation field $A(x, y)$ is homogeneous, one can use Eq. (12) to predict the performance of CFT in estimating the pointing-induced bias v_p by replacing M with the approximate equivalent number of independent samples, calculated as

$$M_{\text{eq}} = \Delta x \text{ PRF } K/v_s, \quad (16)$$

where K is a shape factor for $D_m(x)$, for a Gaussian shape $K = 2\pi^{0.5}$. For the configuration considered here,

one obtains $M_{\text{eq}} = 4000$, which, through Eq. (12), would satisfy the requirements imposed in section 2. While simulations performed under these assumptions confirmed the validity of this approach, more realistic simulations such as those discussed in the next section are necessary to provide a better insight in the expected performance of CFT.

5. Results and discussion

Doppler spectra measured by NDPR have been obtained through a 3D Doppler radar simulator (Tanelli et al. 2002) that divides each radar volume of resolution into many subvolumes and combines the returns of all subvolumes by weighting their contributions accordingly to the weighting function $W(\mathbf{r})$. The simulated radar signal for the radar cells close to the surface includes the direct return from the sea surface, the direct return from raindrops, and the mirror image return of the raindrops (the radar signal generated by raindrop scattering within the radar volume intersecting the surface is a source of error in estimating the surface Doppler spectrum and was included for completeness of our performance analysis). The radar-return signal from the sea surface is modeled as a zero mean Gaussian process because the size of the footprint (2.2 km) is much larger than the correlation length of sea surface roughness (up to 60 m for waves generated by winds up to 20 m s^{-1} , and a few centimeters for rain-generated roughness), and the ratio between the coherent and incoherent components of the surface return is close to zero for a 14-GHz nadir-looking radar in good accordance with the extremely rough surface approximation, even for the rms roughness of surface height $\sigma_h = 1$ cm (see appendix A). The value of the normalized radar cross section corresponding to each subvolume intersecting the sea surface was calculated accordingly to a polynomial function fitting the results of the full-wave model described in Capolino et al. (1998).

The simulator was applied to 3D fields of hydrometeors and wind generated by a cloud resolving model (CRM), and to 3D rainfall and vertical velocity fields measured by the National Aeronautics and Space Administration (NASA) Jet Propulsion Laboratory (JPL) Airborne Rain Mapping Radar (ARMAR; Durden et al. 1994). The spacecraft attitude errors were simulated by a stochastic process with a bandwidth B_Θ ranging from 0.1 to 1 Hz, and a non-Gaussian low-pass shape.

Figure 5 describes the case study relative to a tropical squall line generated by the CRM using initialization inputs from sounding measurements gathered during the Tropical Ocean Global Atmosphere (TOGA) Coupled Ocean–Atmosphere Response Experiment

TABLE 2. Retrievals of vertical velocity from NDPR for a CRM-generated tropical storm. All statistics are expressed in meters per second. The CFT/CFT technique uses CFT to estimate the pointing-induced bias v_p as well as the vertical rainfall velocity, DFT/CFT differs in that it uses DFT to estimate v_p , and NO/CFT does not estimate v_p at all. The results for v_p (in italics) refer to the estimates of pointing-induced bias; those labeled v_z refer to the corresponding estimates of rainfall vertical velocity in the radar volumes occupied only by hydrometeors.

Method →	CFT/CFT				DFT/CFT				NO/CFT			
$\Delta x \rightarrow$	700		2800		700		700*		2800		N/A	
	Bias	Rmse	Bias	Rmse	Bias	Rmse	Bias	Rmse	Bias	Rmse	Bias	Rmse
v_p	<i>-0.15</i>	<i>0.43</i>	<i>-0.05</i>	<i>0.40</i>	<i>-1.97</i>	<i>2.97</i>	<i>-1.58</i>	<i>4.32</i>	<i>-1.58</i>	<i>0.88</i>	<i>-4.85</i>	<i>2.53</i>
v_z												
All rain volumes	-0.005	0.68	-0.13	0.70	2.38	3.09	0.93	5.04	1.47	1.18	2.96	1.56
0 ÷ 10 dB	0.07	0.95	-0.006	1.00	1.10	1.77	-0.17	3.77	1.23	1.25	2.96	2.00
>10 dB	-0.001	0.66	-0.14	0.67	2.47	3.14	1.01	5.11	1.49	1.17	2.96	1.52

(COARE) measurement campaign. Figure 5a shows the isopleths of mass content of rain (blue shade) and frozen hydrometeors (black) at 0.01, 0.1, 1, 1, and 3 g m⁻³. Figure 5b shows the corresponding reflectivity measurements as obtained by the radar system described in Table 1. The rain-induced attenuation is evident in correspondence of the four rain cells located at 22, 29, 37, and 43 km in the along-track coordinate. In particular, note that the rain signal is lost in the range bins close to the surface in the first rain cell. Figure 5c shows the true reflectivity-weighted vertical velocity of the hydrometeors. This case study is representative of precipitating systems with extreme convection, very pronounced NUBF, and very large attenuations. The pointing error was simulated assuming a 0.1-Hz bandwidth in the torque spectrum $\Theta(f)$, and it resulted in an average mispointing of 39×10^{-3} degrees aft with a standard deviation of 20×10^{-3} degrees in the 10-s interval relative to the whole case study. The pointing-induced velocity bias is represented by the solid black curve in Fig. 5d; the average bias is $v_p = 4.8 \text{ m s}^{-1}$, with an rms of 2.5 m s^{-1} and a maximum rate of change of 0.6 m s^{-2} . The red and blue solid curves represent the pointing-induced bias that is estimated by analyzing the sea surface radar echo through CFT and DFT, respectively. In both techniques, the width Δx of the along-track Gaussian window used for averaging was set to 2800 m [$D_m(x)$ approximately equivalent to four radar footprints]. CFT estimates of the pointing-induced bias v_p have an rmse of 0.4 m s^{-1} , and those obtained with $\Delta x = 700 \text{ m}$ (dashed red curve, almost overlapped to the solid red curve in Fig. 5) are deteriorated only marginally (see also Table 2). The DFT-estimated profile of v_p includes the correction described by Eq. (15), that is, NUBF is approximated with a constant along-track gradient of apparent surface reflectivity, and such an along-track gradient is calculated by averaging over all of the samples obtained in the along-track direction

within one radar footprint. The resulting rms of 0.89 m s^{-1} is due mainly to localized areas of large error occurring where the constant-gradient assumption made to obtain Eq. (15) is not satisfied. A profile estimated through DFT with $\Delta x = 700 \text{ m}$ and without the correction described by Eq. (15) (hereinafter referred to as DFT*) is shown by a dashed blue curve; it is affected by larger errors induced by large and nonhomogeneous attenuation, swinging from negative to positive errors as the radar beam enters and leaves a rain cell. Such errors affect any standard estimator of the spectral moments (i.e., DFT and PP alike). On the other hand, the negative bias that is visible in DFT estimates in the left-hand side of the storm is induced by spectral aliasing and can be mitigated by adopting a different implementation of the basic DFT or PP algorithms (Tanelli et al. 2004).

The final estimate of the vertical velocity field of the hydrometeors shown in Fig. 5e is obtained first by applying CFT with $\Delta x = 2800$ to the sea surface echo to correct for the pointing-induced bias, and then with $\Delta x = 700$ to the return from precipitation to correct for the NUBF-induced bias. The performance of the technique, indicated hereinafter as CFT/CFT (where this notation stands for the algorithm used to estimate v_p /algorithm used to estimate vertical rainfall velocity), is best seen through the error field shown below, in Fig. 5g. Errors above 1 m s^{-1} occur almost only in areas of very low SNR (cf. to the reflectivity field in Fig. 5b). Intensity and location of updrafts (e.g., at $\sim 20 \text{ km}$ along track, above 5-km altitude) and downdrafts (e.g., at 15 km along track, 13-km altitude) are correctly reconstructed.

The error fields of two alternate approaches are provided in Figs. 5f and 5h. The two approaches differ from CFT/CFT only in the technique that is used to estimate and correct for the pointing-induced bias. The DFT/CFT technique (shown in Fig. 5f) corrects the pointing-

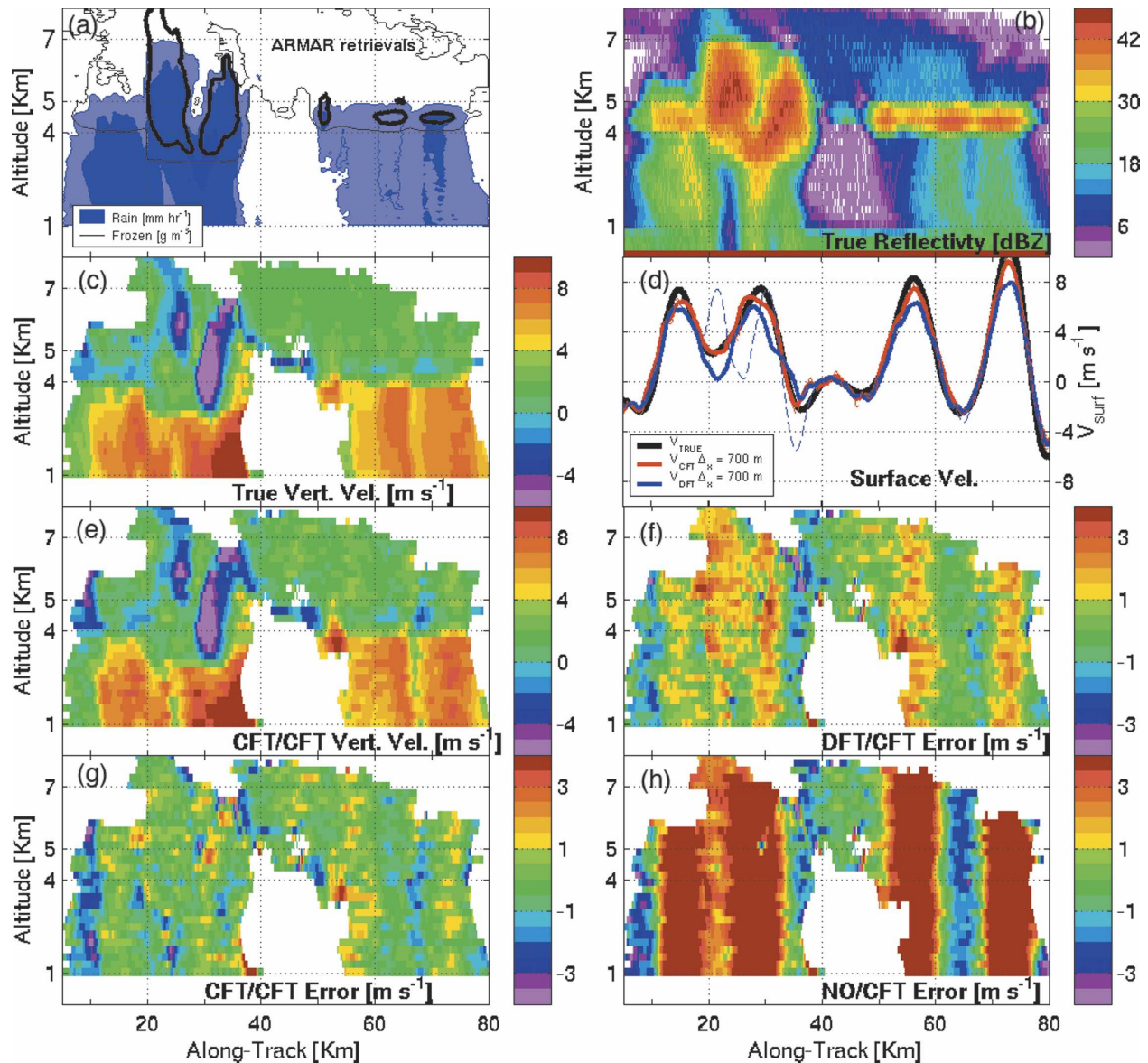


FIG. 6. Retrievals of vertical velocity from NDPR for an ARMAR-retrieved tropical storm: (a) equivalent mass liquid content for frozen hydrometeors (black, thin at 0.01 g m^{-3} and thick at 0.1 g m^{-3}) and rain rate (blue shades with transitions at $0.1, 1$, and 10 mm h^{-1}), and (b)–(g) same as in Fig. 5.

induced error through DFT analysis of the sea surface (with $\Delta x = 2800$). The results of the DFT/CFT method are comparable to those of the CFT/CFT method where moderate attenuation occurs, but they are seriously compromised in presence of strong convective rain cells (e.g., around 20 km along track). The last approach, named NO/CFT, simply ignores the pointing-induced bias, which is, therefore, evident throughout the whole error field in Fig. 5h.

The statistics of the retrievals shown in Fig. 5 are shown in Table 2. The first row shows the bias and rmse in estimating the pointing-induced velocity v_p through

CFT (in the CFT/CFT columns) and DFT (in the DFT/CFT columns). Results are shown for two separate values of Δx (i.e., $\Delta x = 700 \text{ m}$ and $\Delta x = 2800 \text{ m}$); the column labeled 700* shows results obtained using the DFT* version of the DFT algorithm to estimate v_p . These results show that the correction described by (15) is indeed reducing the rmse at the expense of a small deterioration in bias, however, the overall performances of DFT for this case study are significantly worse than those achieved through CFT because of the large effect of nonuniform attenuation. The NO/CFT columns show the error statistics in v_p estimates when

TABLE 3. Retrievals of vertical velocity from NDPR for an ARMAR-retrieved case study. Symbols are as in Table 2.

Method →	CFT/CFT				DFT/CFT				NO/CFT			
$\Delta x \rightarrow$	350		700		350		700*		700		N/A	
	Bias	Rmse	Bias	Rmse	Bias	Rmse	Bias	Rmse	Bias	Rmse	Bias	Rmse
v_p	0	0.73	-0.01	0.70	-0.4	1.16	-0.36	1.61	-0.41	1.03	-1.5	4
v_z												
All rain volumes	-0.15	1.08	-0.14	1.04	0.48	1.26	0.41	2.07	+0.50	1.26	+2.73	3.30
0 ÷ 10 dB	-0.03	1.20	-0.05	1.19	0.41	1.20	0.39	1.98	+0.46	1.24	+2.12	3.50
>10 dB	-0.21	1.02	-0.19	0.96	0.50	1.28	0.43	2.11	+0.52	1.26	+3.03	3.15

v_p is simply assumed to be zero (i.e., the statistics of true v_p).

The three rows at the bottom of Table 2 show the corresponding statistics of the vertical rain velocity retrievals obtained after shifting the Doppler spectra by the estimated v_p . These sets of statistics were calculated over the whole dataset (indicated by “all rain volumes” in Table 2), as well as on the two subsets discriminated by a threshold of 10 dB in SNR. As shown in Tanelli et al. (2004), rmse of CFT results depends mainly on the SNR level of each rain volume (qualitatively, rmse decreases with increasing SNR approximately up to the 10-dB level where it settles asymptotically to the “large SNR” rmse value). This is confirmed in the results of the CFT/CFT technique. On the other hand, DFT/CFT and NO/CFT estimates are clearly affected by the comparatively larger error in the v_p estimates (which are independent of the SNR level of each rain volume) and, therefore, do not exhibit a clear dependence on an SNR level.

Figure 6 describes a case study relative to ARMAR observations of a convective cell embedded in a stratiform system during the Kwajalein Experiment. The isopleths in Fig. 6a are at 0.1, 1, and 10 mm h⁻¹ for rain and 0.01 and 0.1 g m⁻³ for frozen particles. In this case, the oscillations of the spacecraft were modeled with a bandwidth of 1 Hz, resulting in an average mispointing of 12×10^{-3} deg aft with a standard deviation of 30×10^{-3} deg. The corresponding average bias is $v_p = 1.5$ m s⁻¹, with an rms of 4 m s⁻¹ and a maximum rate of change of 16 m s⁻². The solid curves in Fig. 6d show DFT and CFT estimates of the apparent surface velocity obtained with $\Delta x = 700$ —the former has a 0.41 bias and 1.03 rmse, the latter has an almost 0 bias and 0.70 rmse. The dashed blue curve shows DFT* results (with $\Delta x = 700$ m). This case shows smaller NUBF-induced errors than the previous case study because of the lower rainfall intensity (and, therefore, smaller attenuation) in the rain cell. On the other hand, filtering introduced by $D(x)$ tends to smooth out the relatively high frequency oscillations, causing localized areas of large er-

ror (visible as vertical error bands in Fig. 6f). Results obtained by setting $\Delta x = 350$ m show somewhat better performance in tracking the profile of oscillations at the expense of an increase in ripple caused by the signal noisiness (see statistics in Table 3).

These results indicate that a 1-Hz bandwidth in the torque spectrum could be considered as a limit for the NDPR configuration considered in this paper. Also, CFT performances degrade gradually with increasing bandwidth and each configuration should be assessed independently.

6. Conclusions

The use of spaceborne Doppler radars in low earth orbit to measure the vertical velocity of rainfall requires knowledge of the antenna-pointing angle within few arcseconds. Such a stringent pointing requirement could pose a technical challenge to the spacecraft-pointing determination instrumentations. This paper describes a combined frequency–time (CFT) processing algorithm, which provides the required level of pointing knowledge without the need of imposing the tight requirement on spaceborne instrumentations.

When a homogeneous rainfall field is observed, the pointing-induced bias is given by the first moment of the Doppler spectrum of the surface echo. However, when NUBF occurs in moderate to heavy rain, the radar signal is not uniformly attenuated within the footprint. It follows that the first moment of the Doppler spectrum of the sea surface is a biased estimate of the pointing-induced error. This NUBF-induced bias can amount to several meters per second for a LEO satellite.

Application of the new CFT algorithm to the sequence of measured Doppler spectra of the sea surface enables the correction of the NUBF-induced bias and, therefore, allows for the successful estimation and removal of the pointing-induced bias from the rainfall vertical velocity measurements. Our model simulation results show that, for the radar configuration consid-

ered in this study, CFT is effective in removing frequency components of the pointing error below 1 Hz, and that overall accuracy of 1 m s^{-1} or better can be achieved even when extremely strong convective cells are present.

The results obtained through CFT were compared to those obtainable through standard spectral moments estimators once a simplified model to correct for NUBF-induced biases is implemented. This second approach guarantees acceptable results in moderate NUBF conditions, but its performances are more sensitive to the accurate estimation of the bandwidth of the pointing oscillations and the presence of strong convective cells that are smaller than the radar footprint.

The results presented in this paper for a nadir-pointing radar system can be extended, in principle, to a cross-track scanning radar; however, increasing the number of cross-track beams results in a coarser sampling in the along-track direction. A first approximation of the corresponding degradation in CFT performance can be evaluated by considering that the number of equivalent samples given in Eq. (16) must be divided by the number of cross-track beams.

Acknowledgments. The research described in this paper was performed at the Jet Propulsion Laboratory, California Institute of Technology, under contract with the National Aeronautics and Space Administration, and by the University of Firenze through a program funded by ASI (Italian Space Agency).

APPENDIX A

Characterization of the Doppler Signal from the Sea Surface

The Doppler spectrum described by Eq. (4) represents the expected power spectrum of the signal backscattered by a rough sea surface. A recent study by Kobayashi and Kumagai (2003) addressed the formal derivation of the total received signal at a spaceborne Doppler radar. Interested readers can find in that paper a rigorous description of the total received Doppler signal. In this appendix, only the conclusions therein that are relevant to this work are briefly summarized.

To confirm the appropriateness of the extreme rough surface approximation, we shall consider the ratio of the coherent power to the incoherent power given by the above approximation, which can be calculated from Ishimaru (1978), or more generally from Kobayashi and Kumagai (2003):

$$\frac{P_c}{P_i} = \frac{2^4 \ln 2 |R_f|^2 \sigma_h^2}{l_c^2 \theta_{3\text{dB}}^2 R_{f0}^2} e^{-4\sigma^2 k^2}, \quad (\text{A1})$$

where R_f and R_{f0} are the reflection coefficients for a smooth and rough surface, respectively, σ_h^2 is the rms roughness of the sea surface, l_c is the sea roughness correlation length, and k is the wavenumber. At Ku band, the ratio in Eq. (A1) tends to be zero even for very small σ_h^2 . For example, if $\sigma_h^2 = 1 \text{ cm}^2$, Eq. (A1) yields $P_c/P_i = 6.8 \times 10^{-10}$. This means that the coherent return can be neglected even for nadir operation and, therefore, the signal can be represented by the extremely rough surface approximation, along with the statistical properties of only the incoherent backscattered signal (i.e., complex zero mean Gaussian process and exponential distribution of power). This result is confirmed by experimental evidence from several airborne radar campaigns. For example, experiments carried out with the NASA JPL ARMAR and Airborne Second Generation Precipitation Radar (APR-2) in the last 10 yr showed anomalous peaks in return power (resulting from the coherent signal from specular reflections) only sporadically over shallow waters adjacent to, and downwind of, atolls. Also, each spectral line obtained from discrete Fourier analysis can be considered independent from the others for the configuration shown in Table 1. In fact, the lines are originated by portions of sea surface that are $\Delta v/q$ apart, where Δv is the Doppler resolution.

APPENDIX B

Complete Derivation of Eq. (3)

In Doppler radars, the Doppler velocity is given by measuring the phase difference between two adjacent pulses/samplings, instead of measuring the direct Doppler frequency shift that is caused by a moving body. The formal derivation of the Doppler velocity from a surface can be found in Kobayashi and Kumagai (2003) and is briefly summarized here.

Suppose that σ denotes the rms roughness of surface, referring to Fig. 1 for the definition of the angles, the coherent surface Doppler velocity is given by

$$v_p^{\text{co}} = v_s \sin \theta_A / \cos \theta_0, \quad (\text{B1})$$

which arises from the change in the beam path because of a platform displacement.

For an extremely rough surface ($\sigma \gg \lambda$), in which the coherent scattering is negligible, the incoherent surface Doppler is given by

$$v_p = v_s \cos \theta_A \sin \theta_0 \cos \phi_0 - v_s \sin \theta_A \sin \theta_0 \tan \theta_0 + v_s \sin \theta_A / \cos \theta_0, \quad (\text{B2})$$

which can be rewritten by merging the last two terms in the right-hand side as

$$v_P = v_s \cos\theta_A \sin\theta_0 \cos\phi_0 + v_s \sin\theta_A \cos\theta_0, \quad (\text{B3})$$

where the two terms on the right-hand side of Eq. (B3) are the projections on the radar-pointing direction of the horizontal and vertical components of the spacecraft velocity, respectively. In vector notation, $v_P = -\mathbf{v}_s \cdot \mathbf{i}_M \cdot \mathbf{i}_V$, which can be expressed in the form of Eq. (3) in the spacecraft motion-referenced system, and is equivalent to that of the incoherent Doppler velocity from random particle scatterers.

When $\sigma \gg \lambda$ is not satisfied (i.e., in rarely observed extremely shallow conditions, see appendix A), the simple form of Eq. (B2) for incoherent surface Doppler

velocity no longer holds; furthermore, the coherent scattering is not negligible anymore. Therefore, the measured Doppler velocity is represented by the linear combination of Eq. (B1) and the incoherent Doppler velocity given by the phase term calculated from Eq. (31) in Kobayashi and Kumagai (2003) weighted by the absolute values of Eqs. (27) and (31) in the same paper.

APPENDIX C

List of Symbols and Acronyms

Table C1 provides a complete list of symbol and acronym definitions and descriptions.

TABLE C1. (a) Symbols used.

Symbol	Definition	Description
$A(x, y)$	$10^{-0.2fk(x,y,z)} dz$	Total two-way attenuation at the surface
$D_m(x)$		Along-track weighting function used in CFT
f_I	$1/T_I$	Cutoff frequency of stability effects
h_s		Satellite altitude
\mathbf{i}_M	See Fig. 1	Spacecraft motion direction
\mathbf{i}_N	See Fig. 1	Zero Doppler direction (it belongs to the orbital plane and is orthogonal to \mathbf{i}_M)
\mathbf{i}_C	See Fig. 1	Cross-track direction (orthogonal to the orbital plane)
\mathbf{i}_x	See Fig. 1	Along-track direction
$-\mathbf{i}_z$	See Fig. 1	Nadir
\mathbf{i}_V	See Fig. 1	Antenna-pointing direction
\mathbf{i}_R	See Fig. 1	Line of sight from spacecraft to generic point
$k(x, y, z)$		One-way specific attenuation (dB km^{-1})
M		Number of samples per spectrum
M_x	$\text{PRF}^2/(q_{xv}Mv_s)$	Number of spectra per target track
PRF		Pulse repetition frequency
$P(x_s, v)$	See Eq. (9)	Theoretical Doppler spectrum of the sea surface
\mathbf{p}_s	(x_s, y_s, z_s)	Satellite coordinates in the fixed coordinate system
q_{xv}	$\sim v_s/h_s$	Doppler shift rate
r		Generic range from radar
\mathbf{r}	$\mathbf{r}_R = (r, \theta, \phi)$	Generic coordinates in the radar coordinate system
\mathbf{r}_V	$r_V \mathbf{i}_V$	Position of the center of the volume of resolution
T_I	M/PRF	Radar observation time
\mathbf{u}		Target velocity vector
u_{surf}		Horizontal wind speed at the surface
v	$-f\lambda/2$	Doppler velocity
\hat{v}		Estimated average vertical velocity
v_{surf}		Apparent velocity of the surface
v_r		Radial (Doppler) velocity
v_P		Velocity bias introduced by pointing angle and platform motion
v_s		Satellite velocity
v_α		Velocity bias due to pointing uncertainty
$W(\mathbf{r}; \mathbf{r}_V)$	$(CG_a^2(\theta, \phi) G_r(r - r_V) ^2/L(r)r^4)$	Radar weighting function, where C is the radar constant, G_a is the antenna gain pattern, G_r is the range weighting function, and L is the atmospheric attenuation
$W_X(x)$	$W(\mathbf{r}, \mathbf{r}_V) = W_X(x - x_V)W_Y(y - y_V)$	Along-track weighting function
$W_Y(y)$	$W_Z(z - z_V)$	Cross-track weighting function
$W_Z(z)$		Vertical weighting function (for the surface range bin $z_V=0$)
x'	$\mathbf{r} \cdot \mathbf{i}_M$	Along-track displacement from zero isodop
$Z_R(\mathbf{p})$	$\int \eta_R(\mathbf{p}, v) dv$	Rainfall reflectivity
$Z_X(x)$	$\int \eta_X(x, v) dv$	Along-track profile of reflectivity
Δx	$h_s \theta_3 [16 \ln(2)]^{-1/2} \cong 0.3 \theta_3 h_s$	Along-track weighting function width parameter
$\eta(x, y; v)$		Natural Doppler spectrum of the surface
$\eta_X(x, v)$	$\int_Y \eta_R(x, y; v) \cdot W_Y(y) W_Z(z) dy dz$	Cross-track-averaged natural Doppler spectrum

TABLE C1. (a) (Continued)

Symbol	Definition	Description
θ_3		Antenna 3-dB (one way) beamwidth
θ_o	See Fig. 1	Pointing elevation off-nadir
ϕ_o	See Fig. 1	Pointing azimuth off-nadir
$\theta_x(t)$	See Fig. 1	Pointing elevation angle (forward-aft component)
θ_C		Pointing control error
θ_α		Pointing uncertainty
θ_A	See Fig. 1	Spacecraft motion elevation angle (off-horizontal)
θ_V	See Fig. 1	Antenna-pointing elevation (from off-zero Doppler)
ϕ_V	See Fig. 1	Antenna-pointing azimuth (off-zero Doppler)
$\Theta(f)$	$\Im\{\theta_x(t)\}$	Torque spectrum (spectrum of antenna-pointing uncertainty)
B_Θ		Torque spectrum bandwidth
λ		Radar operating wavelength
σ_α		Pointing uncertainty rms budget
σ_β		Pointing stability rms budget
σ_h		Rms height of sea surface
σ_θ		Sea surface normalized radar cross section

TABLE C1. (b) Acronyms used.

ADS	Attitude determination system
ARMAR	Airborne Rain Mapping Radar
CFT	Combined frequency-time technique
CRM	Cloud resolving model
DFT	Discrete Fourier transform
LEO	Low earth orbit
NDPR	Nadir-looking Doppler precipitation radar
NUBF	Nonuniform beam filling
PP	Pulse pair
SNR	Signal-to-noise ratio
TOGA	Tropical Ocean Global Atmosphere Coupled
COARE	Ocean-Atmosphere Response Experiment
TRMM	Tropical Rainfall Measuring Mission
UBF	Uniform beam filling

REFERENCES

- Amayenc, P., J. Testud, and M. Marzoug, 1993: Proposal for a spaceborne dual-beam rain radar with Doppler capability. *J. Atmos. Oceanic Technol.*, **10**, 262–276.
- Apel, J. R., 1994: An improved model of the ocean surface wave vector spectrum and its effects on radar backscatter. *J. Geophys. Res.*, **99**, 269–291.
- Capolino, F., L. Facheris, D. Giuli, and F. Sottili, 1998: EM models for evaluating rain perturbation on the NRCS of the sea surface observed near nadir. *IEEE Proc. Radar Sonar Navig.*, **145**, 226–232.
- Curlander, J. C., and R. N. McDonough, 1991: *Synthetic Aperture Radar*. John Wiley and Sons, 657 pp.
- Durden, S. L., E. Im, F. K. Li, W. Ricketts, A. Tanner, and W. Wilson, 1994: ARMAR: An airborne rain-mapping radar. *J. Atmos. Oceanic Technol.*, **11**, 727–737.
- Ishimaru, A., 1978: *Wave Propagation and Scattering in Random Media*. Academic Press, 574 pp.
- Kobayashi, S., 2002: A unified formalism of incoherent, quasi-coherent and coherent correlation signals on pulse-pair Doppler operation for a cloud-profiling radar: Aiming for a space mission. *J. Atmos. Oceanic Technol.*, **19**, 443–456.
- , and H. Kumagai, 2003: Doppler velocity from sea surface on the spaceborne and airborne weather radars. *J. Atmos. Oceanic Technol.*, **20**, 372–381.
- Lee, A. Y., J. W. Yu, P. B. Kahn, and R. L. Stoller, 2002: Space Interferometry Mission spacecraft pointing error budgets. *IEEE Trans. Aerosp. Electron. Syst.*, **38**, 502–514.
- Meneghini, R., and T. Kozu, 1990: *Spaceborne Weather Radar*. Artech House, 201 pp.
- Sabelhaus, P., and Coauthors, 2001: On-orbit ACDS performance of the LandSat 7 spacecraft. *Adv. Astron. Sci.*, **107**, 685–695.
- Sirota, J. M., P. Millar, E. Ketchum, B. E. Schutz, and S. Bae, 2001: System to attain accurate pointing knowledge of the geoscience laser altimeter. *Adv. Astron. Sci.*, **107**, 39–48.
- Tanelli, S., and E. Im, 2004: Spaceborne Doppler Precipitation Radar: System configurations and performance analysis. *Proc. Fourth Int. Asia-Pacific Symp. on Remote Sensing*, Vol. 5654, Honolulu, HI, SPIE, 140–148.
- , —, S. L. Durden, L. Facheris, and D. Giuli, 2002: The effects of nonuniform beam filling on vertical rainfall velocity measurements with a spaceborne Doppler radar. *J. Atmos. Oceanic Technol.*, **19**, 1019–1034.
- , —, L. Facheris, and S. L. Durden, 2004: Rainfall Doppler velocity measurements from spaceborne radar: Overcoming nonuniform beam filling effects. *J. Atmos. Oceanic Technol.*, **21**, 27–44.
- Voth, C., L. K. Herman, C. M. Heatwole, and G. M. Manke, 2001: Attitude determination for the STEX spacecraft using virtual gyros. *Adv. Astron. Sci.*, **107**, 113–132.
- Wertz, J. R., and W. J. Larson, 1999: *Space Mission Analysis and Design*. Microcosm Press/Kluwer Academic Press, 1010 pp.
- Zrnic, D. S., 1979: Estimation of spectral moments for weather echoes. *IEEE Trans. Geosci. Electron.*, **4**, 113–128.